ELSEVIER

Objective landslide detection and surface morphology mapping using high-resolution airborne laser altimetry

J. McKean[a,*], J. Roering[b]

[a] *Department of Geological Sciences, University of Canterbury, Private Bag 4800, Christchurch, New Zealand*
[b] *Department of Geological Sciences, University of Oregon, Eugene, OR 97403, USA*

Abstract

A map of extant slope failures is the most basic element of any landslide assessment. Without an accurate inventory of slope instability, it is not possible to analyze the controls on the spatial and temporal patterns of mass movement or the environmental, human, or geomorphic consequences of slides. Landslide inventory maps are tedious to compile, difficult to make in vegetated terrain using conventional techniques, and tend to be subjective. In addition, most landslide inventories simply outline landslide boundaries and do not offer information about landslide mechanics as manifested by internal deformation features. In an alternative approach, we constructed accurate, high-resolution DEMs from airborne laser altimetry (LIDAR) data to characterize a large landslide complex and surrounding terrain near Christchurch, New Zealand. One-dimensional, circular (2-D) and spherical (3-D) statistics are used to map the local topographic roughness in the DEMs over a spatial scale of 1.5 to 10 m. The bedrock landslide is rougher than adjacent unfailed terrain and any of the statistics can be employed to automatically detect and map the overall slide complex. Furthermore, statistics that include a measure of the local variability of aspect successfully delineate four kinematic units within the gently sloping lower half of the slide. Features with a minimum size of surface folds that have a wavelength of about 11 to 12 m and amplitude of about 1 m are readily mapped. Two adjacent earthflows within the landslide complex are distinguished by a contrast in median roughness, and texture and continuity of roughness elements. The less active of the earthflows has a surface morphology that presumably has been smoothed by surface processes. The Laplacian operator also accurately maps the kinematic units and the folds and longitudinal levees within and at the margins of the units. Finally, two-dimensional power spectra analyses are used to quantify how roughness varies with length scale. These results indicate that no dominant length scale of roughness exists for smooth, unfailed terrain. In contrast, zones with different styles of landslide deformation exhibit distinctive spectral peaks that correspond to the scale of deformation features, such as the compression folds. The topographic-based analyses described here may be used to objectively delineate landslide features, generate mechanical inferences about landslide behavior, and evaluate relatively the recent activity of slides.
Published by Elsevier Science B.V.

Keywords: Landslides; Surface morphology; LIDAR

* Corresponding author. Now at: USDA Forest Service, Rocky Mountain Research Station, 316 E. Myrtle Street, Boise, ID 83702, USA. Tel.: +1-208-373-4383; fax: +1-208-373-4391.
   E-mail address: jmckean@fs.fed.us (J. McKean).

1. Introduction

Landsliding is a geologic process that occurs over a wide variety of spatial and temporal scales in many mountainous landscapes. Landslides have a corre-

spondingly wide range of effects that depends strongly on their spatial pattern of occurrence and frequency and magnitude of movement (e.g. Palmquist and Bible, 1980; Densmore and Hovius, 2000). Mass movements can be the dominant source of erosion responsible for the long-term geomorphic evolution of hillslope morphology (e.g. Anderson, 1994; Schmidt and Montgomery, 1995; Burbank et al., 1996; Cendrero and Dramis, 1996; Hovius et al., 1997; Densmore et al., 1998; Densmore and Hovius, 2000). Over shorter time periods, landslide erosion may cause environmental damage (e.g. Kelsey, 1980; Blaschke et al., 2000) and slides can be a significant local geologic hazard to land use (e.g. Selby, 1993; Schuster, 1996).

A variety of methods has been developed to assess landslide hazards (e.g. Hutchinson, 1995; Aleotti and Chowdhury, 1999) and the environmental and geomorphic consequences of slope failures (e.g. Hovius et al., 1997; Densmore et al., 1998; Densmore and Hovius, 2000). Regardless of the purpose of a landslide investigation or its spatial or temporal scale, project goals normally include at least evaluation of the location and size of slides and estimation of their recent and future activity. Essentially all techniques used at scales beyond very local site investigations incorporate a landslide inventory map developed by surface mapping of existing slides. This fundamental database is compiled partly as a result of the maxim that future landslides are most likely to occur in conditions similar to those that have caused past failures (Varnes et al., 1984). There is also a need to calibrate models of future landslide hazard and risk with the mapped population of existing landslides.

While mapping may define spatial patterns of landslides, the temporal component of slide activity is more problematic (Lang et al., 1999). Lacking absolute age control from tephras, ^{14}C, etc., mapped landslide surface morphology can sometimes be used as a surrogate for age and/or recent activity. Simply put, more recently active slides are generally rougher with better-developed local morphologic features, such as cracks and interior scarps, etc. (Wieczorek, 1984; Gonzalez-Diez et al., 1999).

Maps of spatial and temporal patterns of the surface deformation of landslides can also be used to investigate individual slide kinematics and mechanics. Fleming and Johnson (1989) used detailed maps of cracks and other surface features at two landslides to define internal elements within the slides, estimate the rheologic properties of the slide materials, and investigate the shapes of the failure surfaces. Hutchinson (1995) observed that the surface morphology of existing slope failures can reveal the type of landslide, which in turn may help predict future behavior, such as velocity, pattern of response to rainfall, likely travel distance, etc. Baum and Fleming (1991) monitored changes over time in zones of longitudinal extension and compression in landslides and used those mapped patterns to predict driving and resisting elements in the slides and constrain the interslice forces employed in limit equilibrium analyses. Baum et al. (1993) also used 3 years of surface deformation monitoring and mapping to investigate a variety of kinematic aspects of a slide, including patterns and homogeneity of longitudinal strain, surface deformation styles caused by extension and contraction and the effects of failure surface geometry on surface deformation.

Methods of landslide mapping have changed little, in principle, over the past few decades even when newer data sources are used. In sparsely vegetated terrain, landslides are routinely detected and mapped by a combination of interpretation of airphotos or multispectral digital imagery and selective ground verification. However, it is quite difficult to use these methods in rugged terrain covered with dense vegetation. In particular, vegetated older dormant slides with subdued topographic expression may be unrecognizable on airphotos or multispectral digital imagery (e.g. Wills and McCrink, 2002). Also, landslide inventory mapping studies typically focus on outlining slide boundaries and neglect the wealth of information revealed by internal deformation features.

We report results of a new approach that exploits measurements of local topographic roughness to detect and map deep-seated landslides. The surface morphology of a landslide complex near Christchurch, New Zealand is characterized with high resolution DEMs produced from LIDAR data. Statistical, Laplacian, and spectral analyses of the DEM are used to quantify the local surface roughness. Spatial patterns of roughness are then employed to distinguish slide from non-slide, identify individual morphologic domains within the landslide complex and estimate the relative recent activity of two adjacent domains.

2. Coringa Landslide

The LIDAR test site is a landslide complex, known as the Coringa Landslide, located 65 km north of Christchurch, New Zealand (Figs. 1, 2 and 3). This 50 ha landslide occurs in the Loburn and Ashley Mudstones, both of which are smectitic, and the Waipara Greensand. These three Paleocene age units have been faulted and folded into position, although the details of the fault relationships are obscured by the slide (Barrell, 1989; Justice, 1994). The Oligocene age Amuri Limestone overlies the mudstones and the

greensand. Barrell (1989) and Justice (1994) both suggest that the landslide was probably ultimately caused by hillslope base level lowering during incision of the Motunau River at the foot of the slope. Progressive slide movement has deflected the river to the south and the long profile of the channel shows a pronounced knickpoint at the landslide.

The local mean annual precipitation is about 700 mm (Moar, 1971). Vegetation on the landslide is predominantly grass with occasional trees and isolated areas of dense shrubs. During the Holocene, the study area was covered with a coastal podocarp forest until
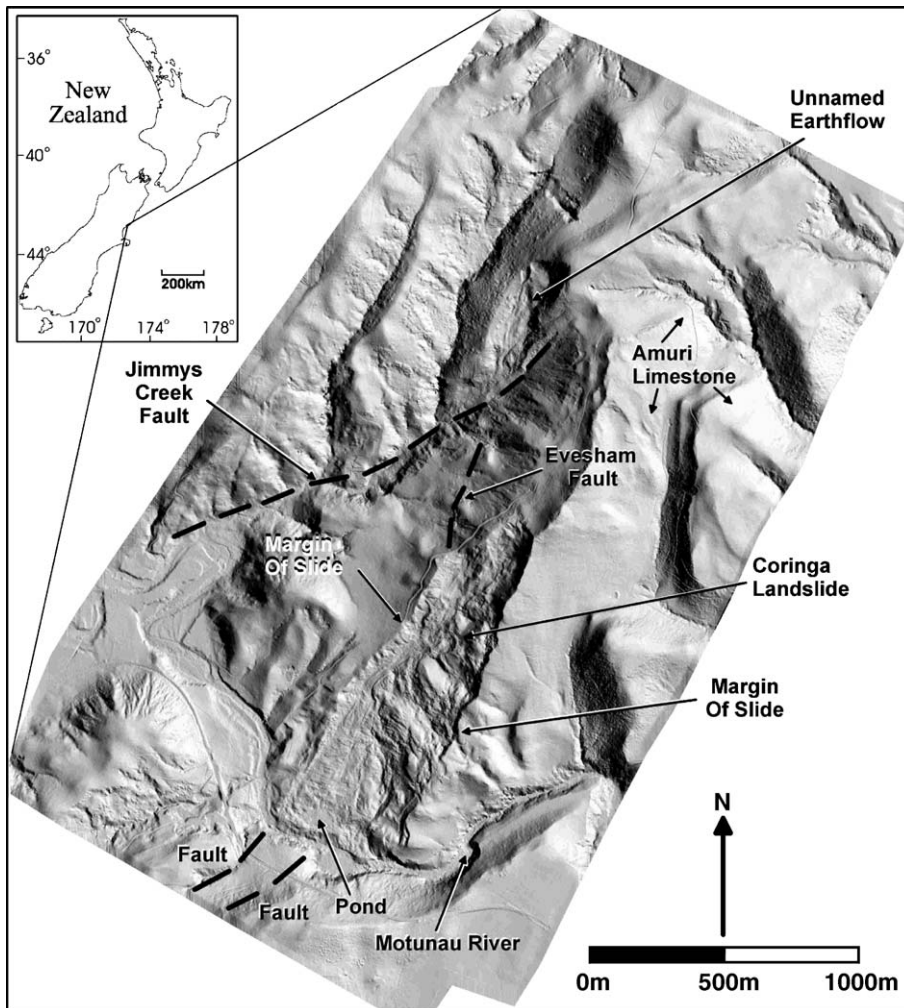

Fig. 1. Location map and shaded relief image of the Coringa Landslide study area. The image was generated from LIDAR data gridded to a density of 1 m.

about 600 years before present when it was converted to grass (Molloy et al., 1963). To focus this project on the development of an objective method to detect and map landslides from a high-resolution DEM, this currently unforested test landslide was used. However, LIDAR has a demonstrated ability to provide topographic data through some vegetation, including some forest canopies (e.g. Kraus and Pfeifer, 1998; Baltsavias, 1999). Thus, the techniques developed here are applicable to forested slides and brief mention is made later of results from smaller forested landslides just northwest of the Coringa Landslide complex.

At present the Coringa Landslide is confined between two well-defined lateral scarps. The eastern scarp is near vertical and exposes up to 30 m of the Amuri Limestone (Fig. 2). The western scarp is also quite distinct but much smaller, and occurs within the Waipara Greensand. East and northeast of the slide intact limestone dips 10° to 25° to the east–southeast, in agreement with the regional structural setting.

The Coringa Landslide has a rich diversity of surficial features. Airphoto interpretation, field mapping and some limited movement monitoring (Barrell, 1989; Justice, 1994) suggest that the majority of the body of the slide is separated into four kinematic units, each of which has a unique morphology (Fig. 3). The eastern side of the landslide is an area of very large slumped blocks (up to 150 m in dimension) of Amuri Limestone and Ashley Mudstone that have become incorporated in the slide and moved slowly south and southwestward from the eastern scarp

(Blocky Area in Fig. 3). Immediately southwest of the Blocky Area are three kinematic units E1, E2 and U1 (Fig. 3). In the field and on airphotos, E1 and E2 appear to be earthflows that are contained within the landslide complex. E1 is visually much smoother than E2, implying less modern activity and some diffusive-like smoothing of the small-scale topographic roughness of this area. Barrell (1989) included a single surface monument in E1 in a monitoring program conducted over a 5-month period. During this time, the movement of the point in E1 was approximately 50% of that recorded in E2.

Earthflow E2 is currently the most active portion of the Coringa Landslide. E2 is about 800 m long with a relatively small modern source area that feeds material into a narrow track along the right margin of the slide complex (Fig. 3). In the past, E2 may have had multiple source areas in the northern portion of the slide complex. The narrow transportation track is only about 20 m wide and falls toward the south at an inclination of about 11%. As material from the source area converges into the narrow track, the velocity increases and the surface of the track is quite smooth. Justice (1994) reports a movement rate of about 2 m/ year over a 24-year period in the track zone. Monitoring during a 12-month period showed a close correlation between rainfall and movement rate in the track and there was about 1.6 m of total movement over that time interval (Justice, 1994). After passing through the track, debris spreads out to a cross-slope width of about 150 m as it accumulates in a lobe of material

Fig. 2. Ground oblique photo of the Coringa Landslide looking north across the Motunau River. The pond in the foreground is just north of a large compression ridge at the toe of the slide. The Amuri Limestone crops out in the cliff on the true left scarp. Modern slide activity is concentrated in the earthflow E2 that lies along the true right margin of the slide and terminates just north of the pond. The surface of E2 is covered with small compression folds generally oriented east-to-west across the earthflow.
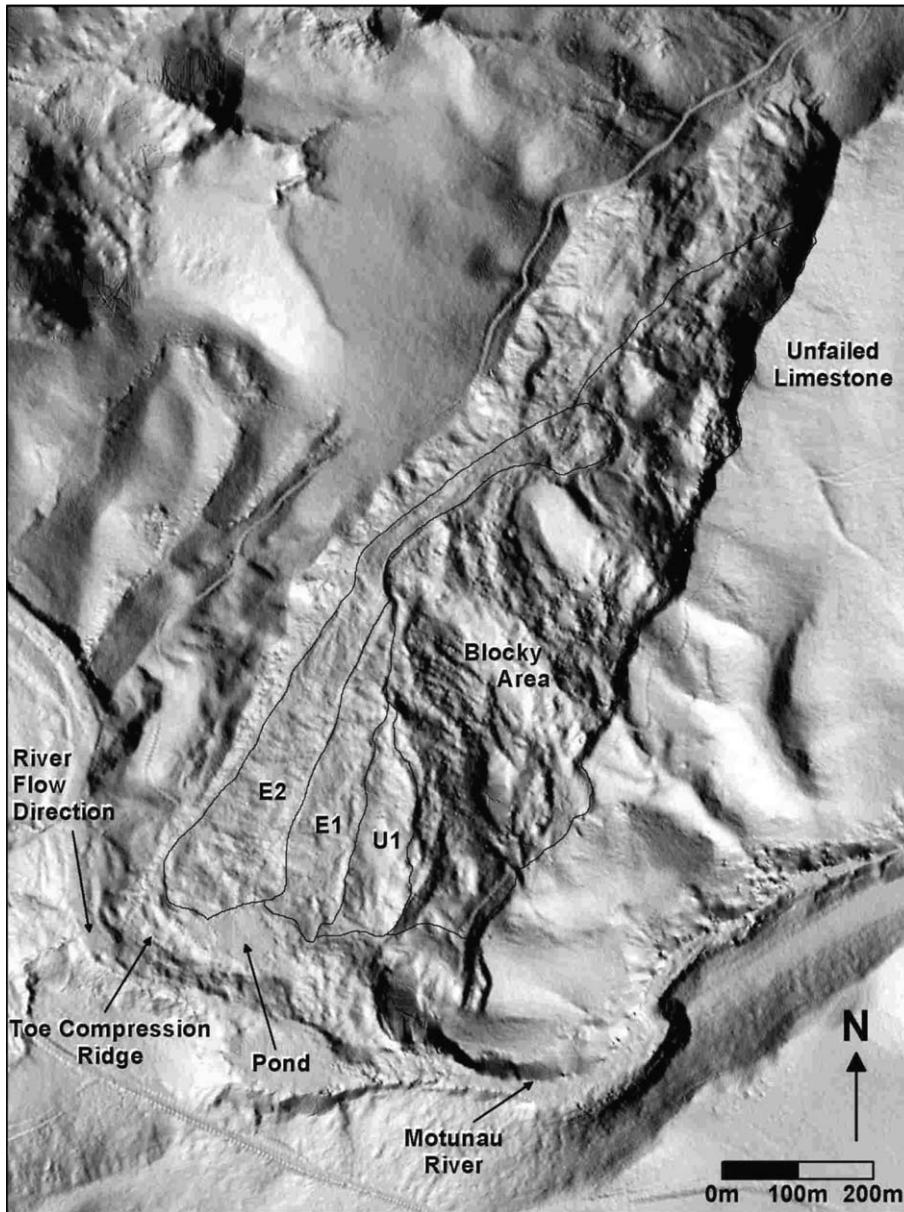
Fig. 3. Shaded relief image of the Coringa Landslide and immediate surroundings. The primary kinematic units within the slide are earthflows E1 and E2, the area of compression U1 and the Blocky area with incorporated limestone blocks.

that extends downslope to near the toe of the slide. Over the same 12-month monitoring period, the average movement in the accumulation zone was about 0.7 m (Justice, 1994). The debris is in compression (N–S) as it collects on the gentler slope (about 8%) of the accumulation lobe, which is buttressed against a large transverse compression ridge at the toe of the slide (Fig. 3). In the southeastern corner of the slide, this ridge has begun to fail into the river channel in a series of localized rotational failures. The surface of the active depositional lobe in E2 is covered with small folds that are generally oriented transverse

to the slide movement (Fig. 2). The wavelength of the folds is 10 to 15 m and their amplitude is 0.5 to 1.5 m. The boundaries of E2 are very distinct with multiple sets of longitudinal levees on both lateral margins. These levees are approximately the same size as the transverse folds and typically are quite straight for distances up to 100 m. The levees are often separated along their margins, and occasionally in their interior, by quite straight tear faults and lateral shears.

Both Barrell (1989) and Justice (1994) argue that U1 is another inactive earthflow lobe that has been separated from its source by southwestward movement of the Blocky Area of the slide. The roughness analysis presented below suggests that U1 is instead a compression ridge in front of large limestone blocks that are converging in this area as they approach from the north and east. A more extensive monitoring system has recently been established to document the absolute and relative movement patterns of U1, E1 and E2. Preliminary monitoring results indicate that both U1 and E1 are moving one to two orders of magnitude slower than E2. The monitoring network has not been established long enough to conclusively document the directions of movement in U1 and E1.

3. Laser altimetry

LIDAR data were obtained with an average density of one laser strike per 2.6 m in six flight lines over the landslide and surrounding area. There was about 20% overlap between the data swaths and all data were georeferenced to the New Zealand Map Grid projection using a global geoid model. There were slight systematic vertical offsets in the data of about ± 15 cm between flight lines as normally occurs in LIDAR surveys. The source of this inaccuracy is uncertain but has generally been ascribed to errors in data from the aircraft GPS and inertial navigation systems or misalignments in the laser optics (Latypov, 2002). For example, as Latypov (2002) states, with a LIDAR system that uses a 1 Hz GPS and 20 kHz laser, a single random GPS error will cause a systematic shift in 20,000 LIDAR data points.

The systematic errors were reduced using the following manual procedure. For each separate flight line, a data grid with constant grid spacing was constructed from the LIDAR data. The gridded data were then contoured, again in separate flight lines. Then the elevations of the data in the flight line most centered on the landslide were adjusted vertically until there were minimal errors relative to ground control profiles and spot elevations. Next, the original data in the two flight lines adjacent to the central line were adjusted vertically until they matched the center flight line. These adjustments were done both by matching elevation contours in the 20% overlap zones and matching ground control data. No horizontal adjustments were made. This process was then repeated with the remaining three flight lines. The original x, y, z data of the now vertically corrected flight lines were then combined and gridded (Fig. 1).

Such systematic relative swath errors can be more easily removed during routine data processing if some flight lines are flown perpendicular to the main group of flight swaths and the orthogonal lines of data are used to remove the relative errors in data from the other flight lines. Latypov (2002) discusses an automated procedure for this purpose that minimizes the offsets of small surfaces in areas of overlap between adjacent and orthogonal flight lines. Cross lines of data were not available in this project.

The ground control data used to reduce systematic errors included one NE–SW profile surveyed by GPS down the middle of the slide complex and three NW–SE profiles, surveyed using an EDM, across the slide and into the smooth terrain adjacent to both sides of the slide. Data were collected about every 10 m in all four profiles. A stratified random sampling scheme was used to also evaluate the spot accuracy of LIDAR data in the smooth terrain outside the landslide and all of the kinematic units within the slide. These random individual control points included 250 measured with GPS and 150 obtained with an EDM. A formal accuracy assessment of the data (raw and processed as just described) is being conducted using these control data (McKean and Roering, in preparation).

4. Statistical measures of surface roughness

The surface of most landslides is rougher, on a local scale of a few meters, than adjacent unfailed slopes. This characteristic can be exploited to automatically detect and map landslides in landscapes

depicted by high resolution DEMs. One technique to quantify local topographic surface roughness is to measure the variability in slope and aspect in local patches of the DEM (Fig. 4). In this approach, unit vectors are constructed perpendicular to each cell in the DEM. The vectors are defined in three dimensions (using polar coordinates) by their direction cosines: $x_i = \sin\theta_i\cos\phi_i$, $y_i = \sin\theta_i\sin\phi_i$ and $z_i = \cos\theta_i$, where θ_i is the colatitude and ϕ_i is the longitude of a unit orientation vector. Local variability of vector orientations is then evaluated statistically. Orientation statistics were calculated in small sampling windows of a fixed size that were moved over the DEM produced from laser altimetry data. By calculating, at each DEM grid cell, the statistical variability of orientation of the unit vectors of all cells in the sampling window, the elevation matrix was replaced with a map of local topographic roughness. Both circular and square sampling windows were evaluated with no apparent difference in results. The effect of the size of sampling window was also tested by varying the window width between 3 and 11 cells and varying the grid cell dimensions between 0.5 and 5 m.
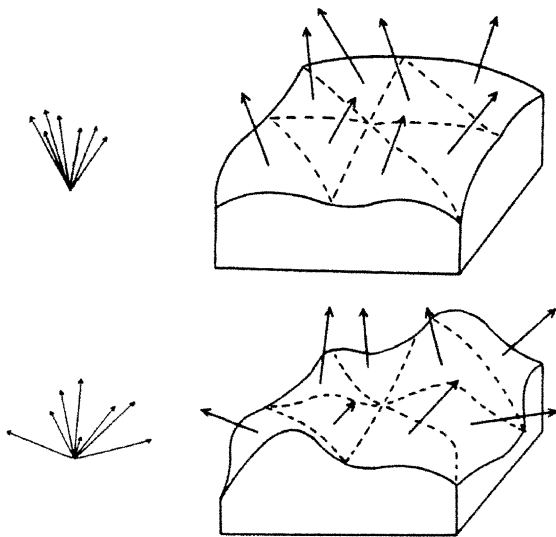

Fig. 4. Topographic surface roughness in a DEM as revealed by unit direction vectors. In smooth topography (top drawing) the local vectors have similar orientations. In rough terrain, as commonly occurs in bedrock landslides, the local vector orientations are highly variable. Modified from Hobson (1972).

4.1. Direction cosine eigenvalue ratios

A variety of statistical measures were investigated to evaluate the local variability of unit vector orientations. The most generally useful of these is the method of eigenvalue ratios. If $(x_1, y_1, z_1)...(x_n, y_n, z_n)$ is a collection of n unit vectors (perpendicular to n topographic pixels), then the orientation matrix, **T**, of the vectors may be formed from the sums of cross products of the direction cosines of the vectors (Fara and Scheiddegger, 1963; Scheidegger, 1965; Watson, 1966; Fisher et al.,1987):

$$\mathbf{T} = \begin{pmatrix} \sum x_i^2 & \sum x_i y_i & \sum x_i z_i \\ \sum y_i x_i & \sum y_i^2 & \sum y_i z_i \\ \sum z_i x_i & \sum z_i y_i & \sum z_i^2 \end{pmatrix}. \tag{1}$$

The eigenvalues (λ_1, λ_2, λ_3) of the matrix describe the amount and nature of clustering of vector orientations (Woodcock, 1977; Woodcock and Naylor, 1983). If the three eigenvalues are normalized with respect to n, then $S_i = \lambda_i/n$ and $S_1 + S_2 + S_3 = 1$. Because there are only two independently varying S_i, the ratio of S_2/S_3 can be plotted against S_1/S_2 to describe the pattern of vector orientations, ranging from clusters to girdles (Fig. 5). The logarithms of the ratios of normalized eigenvalues are calculated and plotted because the ratio values are often not normally distributed. When $S_1 > S_2 \cong S_3$, the orientation data are clustered and alternatively if the data form a girdle, $S_1 \cong S_2 > S_3$. The ratio $\ln(S_1/S_3)$ can also be plotted in the same graph to describe the strength of any orientation without specifying the orientation pattern. If the data have a perfectly uniform distribution, then $S_1 = S_2 = S_3 = 1/3$ and the data would plot at the origin of the graph. Samples with widely dispersed vector orientations may approach this condition.

Fig. 6 shows the eigenvalue ratio of $\ln(S_1/S_2)$ calculated in a three cells-by-three cells sampling window on a DEM with a grid spacing of 3 m. As discussed, this ratio describes the tendency for the vector data to be clustered. Fig. 6 illustrates that over a length scale of 9 m the local orientations of topographic pixels inside the Coringa Landslide are much less clustered than those in the surrounding terrain
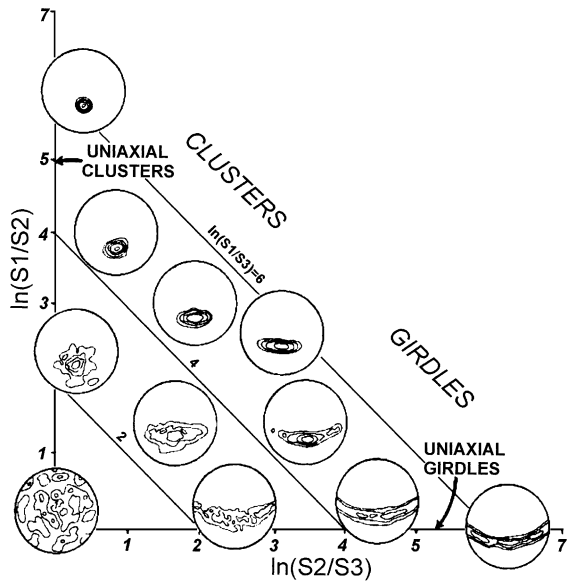
Fig. 5. Normalized eigenvalue ratios of directional data. The ratio $\ln(S_1/S_2)$ predicts the degree of data clustering and $\ln(S_2/S_3)$ describes the tendency of data to plot in a girdle pattern. The ratio $\ln(S_1/S_3)$ expresses how strongly the orientation vectors are grouped without specifying any pattern of assemblage. Modified from Woodcock (1977).

outside the slide. Using this statistic, essentially the entire landslide is classified as "rough" relative to the surrounding terrain, except the surface of some of the large limestone blocks floating in the eastern portion of the slide. The boundary of the slide is sharply defined by the topographic roughness along the head and lateral scarps.

Another slope failure, the Quarry Landslide on the south side of the Motunau River, has been correctly identified on the basis of its roughness (Fig. 6). Rough topography has also been mapped adjacent to three tributary drainages in the northwestern portion of the study area. The roughness detected along the eastern-most tributary is the site of an earthflow, again in the greensands, that is a smaller version of the Coringa Landslide. The flow style of movement of this landslide is evident from the elongated pattern of roughness elements that are oriented down the local slope. Smaller dip slope failures have also been correctly identified on the northwest sides of the middle and western tributaries. These slides are covered with an approximately 20-year-old pine plantation forest. This demonstrates the ability of the LIDAR to produce

high resolution DEMs beneath some forest canopies, and thus the usefulness of this technique on forested hillslopes where conventional landslide inventory mapping from airphotos is very difficult.

Other rough landscape elements in Fig. 6 include roads, channels and prominent bedrock outcrops. All of these are thin linear elements that would not be confused with a landslide. However, stream terraces in the southwest and a pond at the northern end of the study area are also mapped as rough. In fact, these two areas are unique in that they are mapped as nearly completely rough over a 9-m length scale. They appear rough in our analysis because on very flat terrain, even small topographic variations can cause local changes in pixel aspect of up to 180° between neighboring pixels. Therefore, any statistic that includes pixel aspect direction, as do the eigenvalue ratios, will predict high roughness on flat terrain. As discussed later, this confusion can be avoided by instead evaluating variability only in the third direction cosine, which measures local variations in just topographic steepness.

The separability of the Coringa Landslide and the smaller earthflow to the north from the rest of the landscape north of the Motunau River using $\ln(S_1/S_2)$ is described statistically in Fig. 7. The river terraces and the pond have been excluded in this analysis. The histograms and box plots both illustrate the unique-ness of the earthflows. There are few very smooth areas within the slides where $\ln(S_1/S_2)$ exceeds a value of about 2.5. In contrast, much more of the landslide terrain is extremely rough, with $\ln(S_1/S_2)$ less than 1.0, relative to the surrounding topography.

The laser data can also be explored to investigate the morphologic definition of the kinematic units within a large slide. Fig. 8 shows the $\ln(S_1/S_2)$ calculated for the domains U1, E1 and E2 and a portion of the Blocky unit in the mid to southern portion of the Coringa Landslide. In this image the laser data have been gridded to a spacing of 1 m and then linearly interpolated to a 0.5-m spacing to enhance small and subtle topographic features. This grid spacing is less than would normally be used because the average original laser data spacing is 2.6 m. However, the subset covers only the area of the most regular topography within the slide and careful visual examination of imagery derived from the detailed grid data did not show any obvious
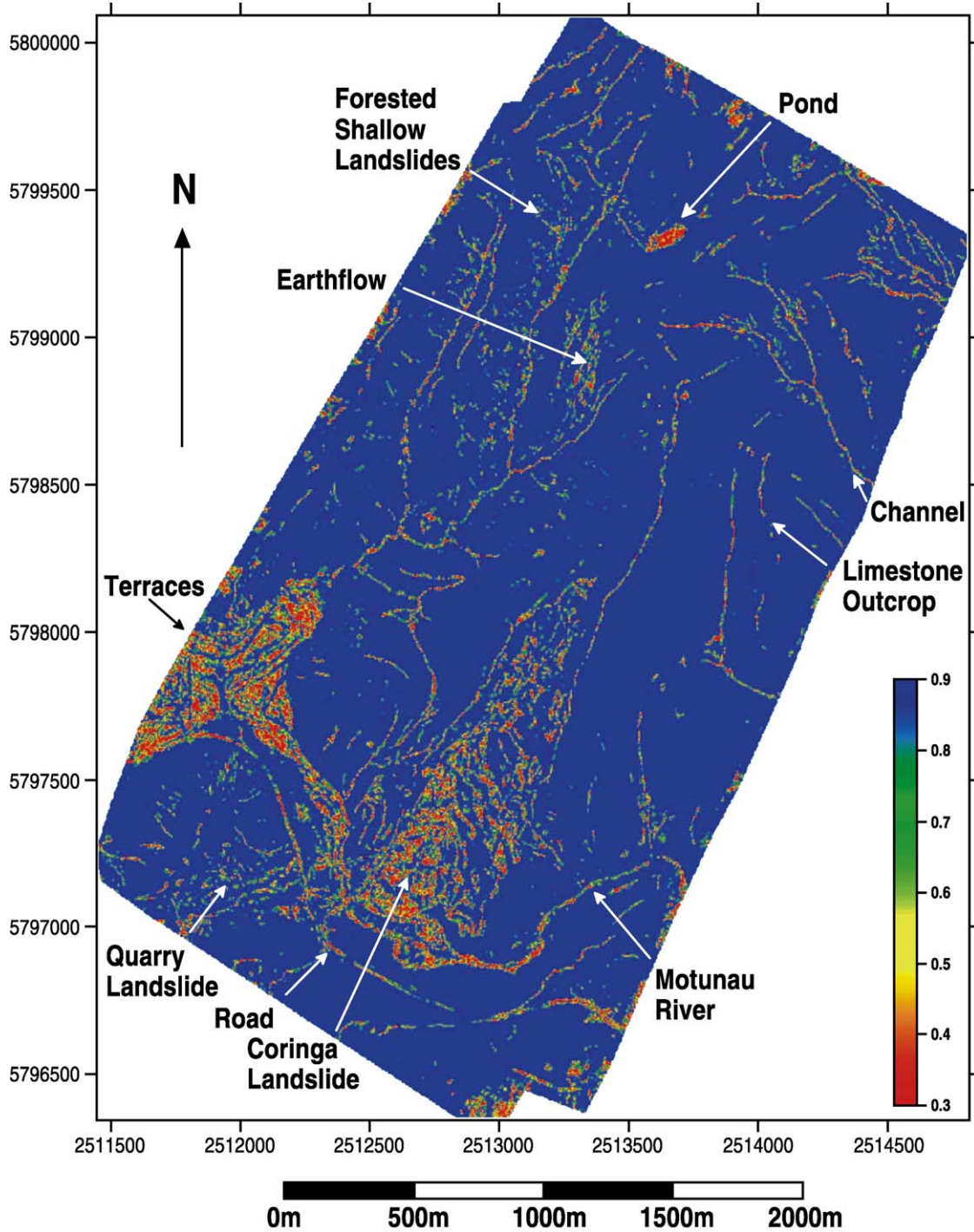
Fig. 6. Eigenvalue ratio $\ln(S_1/S_2)$ calculated in a three cells-by-three cells window on a DEM with a grid spacing of 3 m. Higher eigenvalue ratios indicate smoother topography. The very high values at the pond in the north and the terraces in the southwestern corner are caused by large pixel-to-pixel aspect variations on flat surfaces. The geographic coordinates are in the New Zealand Map Grid system.
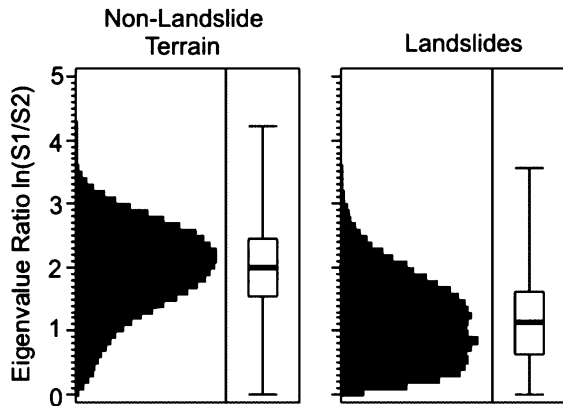
Fig. 7. Histograms and box plots of $\ln(S_1/S_2)$ calculated in a three cells-by-three cells window on a DEM with a grid spacing of 3 m. The top, middle and bottom of each box define the 75, 50 and 25 percentiles, respectively. The rougher topography inside the Coringa Landslide and a smaller unnamed earthflow is distinct from the smoother unfailed portions of the landscape.

gridding artifacts. Experimentation with coarser grids indicated that this amount of detail is necessary to accurately define the small compression folds in E1 and E2, although they can still be detected and approximately mapped using a grid spacing of 1 m.

Within the slide complex, kinematic unit U1 has a median value of $\ln(S_1/S_2)$ of 2.16 and standard deviation (1σ) of 0.74, so this component of the slide is generally quite smooth but with high variability. For comparison, consistently the smoothest terrain in Fig. 8 is the area immediately west of the landslide complex where each DEM pixel is quite similar to its local neighbors. Here the median value of $\ln(S_1/S_2)$ is 2.66 with a standard deviation of 0.67. The earthflow E1 is considerably rougher with a median eigenvalue ratio of 1.86 and 1σ of 0.74 and earthflow E2 is still rougher with a median of 1.76 and 1σ of 0.75. The portion of the Blocky unit that is just east of U1 in Fig. 8 has a roughness comparable to U1 (median eigenvalue ratio 2.17 with 1σ of 0.77). The explanation is that this area of the Blocky unit is composed of very large limestone

blocks whose sides are quite smooth, so the overall surface roughness is low. In other parts of the Blocky unit, particularly near the head and left lateral scarps where limestone blocks have fallen from the scarps, the rock has disintegrated into pieces with dimensions on the order of meters and the local surface roughness is extremely high. In these areas, the existing LIDAR data could not be processed to a grid spacing of 0.5 m without large errors.

In addition to changes in the overall roughness between units in the landslide complex, the spatial patterns or texture of roughness also vary. The interior of E2 is dominated by the many small folds that are generally oriented NW–SE, approximately perpendicular to the direction of slide movement. The eigenvalue ratio $\ln(S_1/S_2)$, as colored in Fig. 8, does not distinguish between convex upward or concave upward topographic forms; i.e. both fold crests and the troughs between adjacent folds are evaluated as extremely rough with low values of $\ln(S_1/S_2)$ (≤ 0.7). The true left and right margins of E2 are marked by multiple generations of longitudinal levees whose positions can be mapped to within 1 to 2 m in Fig. 8. The toe of unit E2 is sharply defined by a curved line of topographic roughness that passes just north of the pond on the landslide (see Figs. 2 and 3 for the location of the pond).

The pattern of roughness is much more disorganized in E1 and the dominant NW–SE trend of folding in E2 is missing. The folds in the interior of E1 are also shorter and less continuous. In Fig. 8, the left margin of E1 is slightly less distinct than is the right margin, which borders unit E2. The few roughness elements in U1 appear to trend predominately N–S. This could be explained by compression of this area from the westward movement of the Blocky area of the slide to the east of U1. The eastern contact between U1 and the Blocky area is a quite distinct thin arcuate pattern of high roughness where the Blocky debris appears to be overriding the material in U1 (Figs. 3 and 8).

Fig. 8. Eigenvalue ratio $\ln(S_1/S_2)$ calculated in a three cells-by-three cells window on a DEM with a grid spacing of 0.5 m. The image is of the southwestern portion of the Coringa Landslide. The DEM was produced by gridding the laser data with a spacing of 1 m and then interpolating the grid to a spacing of 0.5 m. Higher eigenvalue ratios indicate smoother topography. The thin linear elements throughout the image are the crests of small compression folds and the troughs between fold crests. The extremely rough area centered on the coordinates 5797070N and 2512620E is a pond on the landslide. The white line in the center of the image is the location of a profile through four compression folds (profile shown in Fig. 11a). An intermittently visible farm track traverses the slide from 5797215N, 2512550E to 5797060N, 2512800E. The geographic coordinates are in the New Zealand Map Grid system.
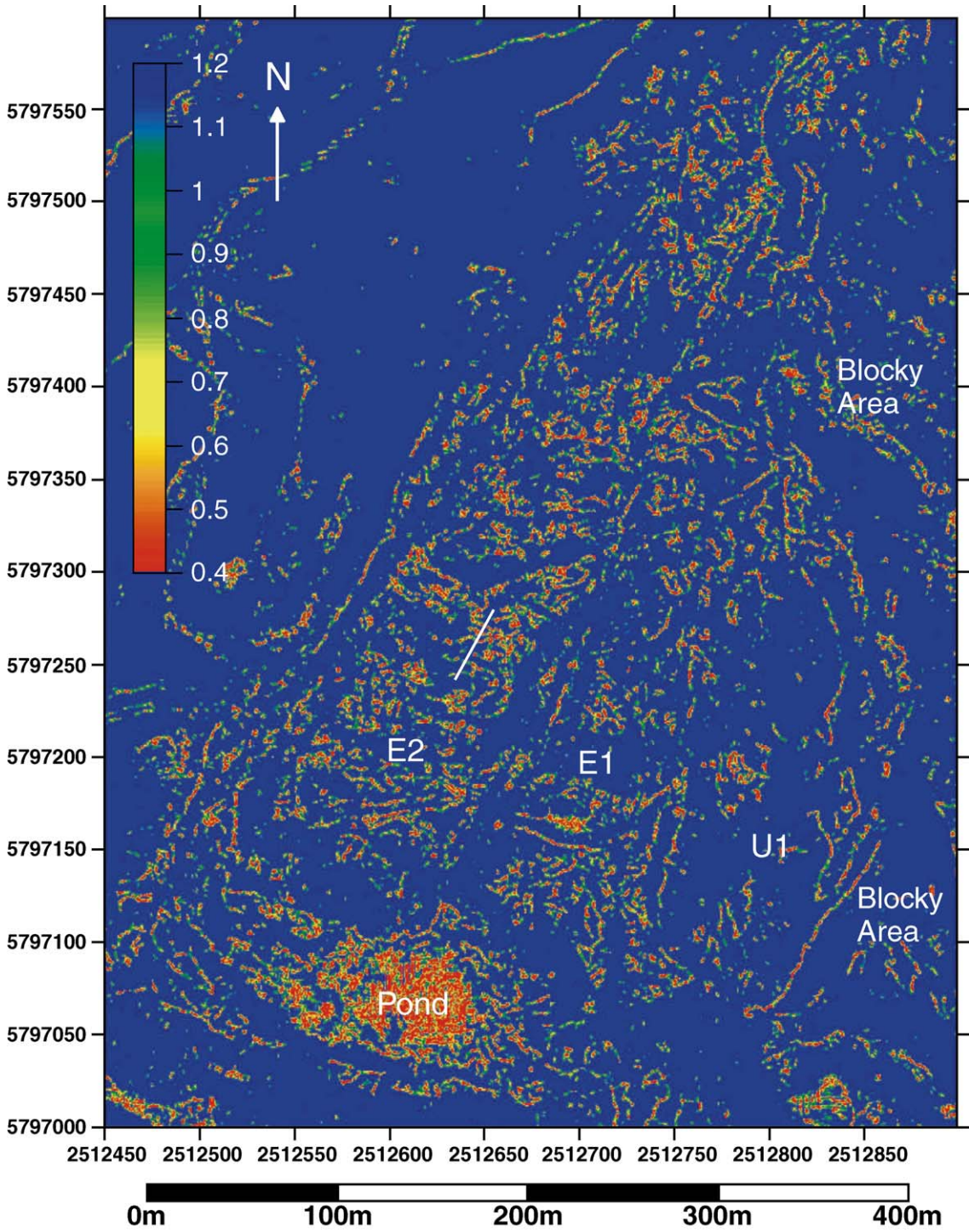
4.2. Other statistics

Several other statistics were also tested, although no roughness maps derived from these are presented. A general discussion of the results from these statistics is included later.

A simple one-dimensional measure of roughness is the local variability of the steepness, or dip, of each digital terrain pixel. This was evaluated using the standard deviation of the gradient of unit vectors in the sampling window. The gradient is expressed as the third direction cosine: $z_i = \cos\theta_i$, where θ_i is the vector dip angle.

Circular statistics can be used to define roughness as two-dimensional variations in topographic aspect. Three related circular statistical measures were evaluated. The magnitude of the mean resultant sum of orientation unit vectors in a local area is calculated as:

$$\overline{R} = \frac{R}{n}. \qquad (2)$$

Here R is the resultant length or the sum of vectors that are normal to n pixels in a sampling window (Fisher, 1993):

$$R = \left(\left(\sum_{i=1}^{n} \cos\theta_i \right)^2 + \left(\sum_{i=1}^{n} \sin\theta_i \right)^2 \right)^{1/2},$$

where $\cos\theta_i$ and $\sin\theta_i$ are the components of the pixel aspect direction. $\overline{R}$ lies in the range $0 < \overline{R} < 1$, where $\overline{R} = 1$ defines a condition in which all vector orientations are coincident. $\overline{R} = 0$ describes greater variability but does not necessarily indicate a uniform distribution of vector orientations. In fact, clustered and poorly distributed orientation vectors can give $\overline{R} = 0$.

Analogous to the standard deviation for linear data is the circular standard deviation that is derived from the mean resultant as (Fisher, 1993):

$$v = (-2\log(\overline{R}))^{1/2}. \qquad (3)$$

Like its linear counterpart, the circular standard deviation varies from 0 to infinity.

The circular dispersion is another two-dimensional measure of data spread that is calculated from the first and second trigonometric moments as (Fisher, 1993):

$$\hat{\delta} = \frac{(1 - \hat{\rho}_2)}{(2\overline{R}^2)}. \qquad (4)$$

Here $\hat{\rho}_2$ is the second trigonometric moment:

$$\hat{\rho}_2 = \left(\left(\frac{1}{n} \sum_{i=1}^{n} \cos2\theta_i \right)^2 + \left(\frac{1}{n} \sum_{i=1}^{n} \sin2\theta_i \right)^2 \right)^{1/2}.$$

The circular dispersion is sometimes used to establish confidence intervals about mean and median values for large samples with $n > 25$ (Fisher, 1993). The circular standard error is related to the circular dispersion by:

$$\hat{\sigma}^2 = \frac{\hat{\delta}}{n}.$$

The mean resultant length of orientation vectors can also be computed in three dimensions (Fisher et al., 1987):

$$R = \left(\left(\sum x_i \right)^2 + \left(\sum y_i \right)^2 + \left(\sum z_i \right)^2 \right)^{1/2}. \qquad (5)$$

Here the meaning of R is the same as for two-dimensional circular statistics.

All statistical measures and eigenvalue ratios that incorporate pixel aspect (the circular standard deviation and dispersion, two and three-dimensional resultants, and eigenvalue ratios $\ln(S_1/S_3)$ and $\ln(S_2/S_3)$), produce results similar to Fig. 8. These statistics are superior in this relatively gentle portion of the landslide because slope angles are never high and the greatest manifestation of topographic roughness is a local change in aspect. In contrast, the one-dimensional standard deviation of the third direction cosine performs poorly in the area show in Fig. 8 because of the lack of steep elements in this gentle terrain. However, the third direction cosine defines more clearly the steep edges of the lateral scarps of the landslide and the edges of blocks in the Blocky unit where the local slopes are up to $90°$.

5. Laplacian operator

An alternative measure that can define topographic features of the kind seen on the surface of bedrock landslides is the Laplacian operator that evaluates the two-dimensional topographic curvature:

$$\nabla^2 z = \frac{\partial^2 z}{\partial x^2} + \frac{\partial^2 z}{\partial y^2}. \qquad (6)$$
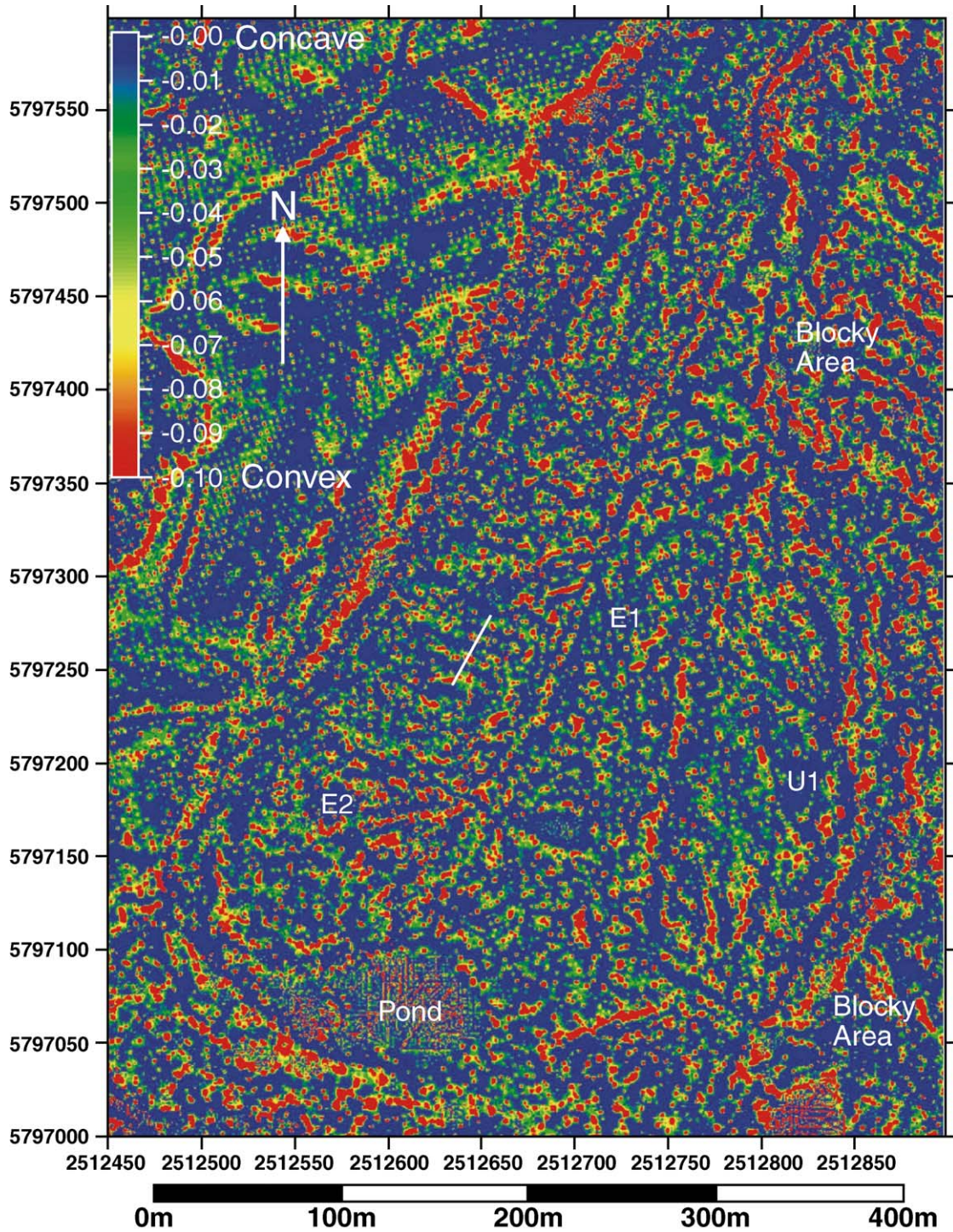
Fig. 9. Laplacian operator calculated on a DEM with a grid spacing of 1 m. The area is the same shown in Fig. 7. The Laplacian was calculated using a five-point central difference algorithm. Warm colors map convex upward morphology. The white line in the center of unit E2 is the location of a profile through four compression folds (profile shown in Fig. 11b). The geographic coordinates are in the New Zealand Map Grid system.

The Laplacian operator was calculated using a standard five-point central difference formula (e.g. Zevenbergen and Thorne, 1987):

$$\nabla^2 z(x, y) = \left[\frac{z_E - 2z + z_W}{\Delta x^2}\right] + \left[\frac{z_N - 2z + z_S}{\Delta y^2}\right].$$

The Laplacian operator was tested on DEMs with a variety of grid spacings and an interval of 1 m provided good spatial resolution while still correctly defining the topographic patterns inside the slide (Fig. 9). This image covers the same portion of the Coringa Landslide shown in Fig. 8. The warm colors represent convex upward morphology and the cool colors correspond to topographic depressions.

The Laplacian operator readily distinguishes the kinematic units U1, E1 and E2 and the boundaries between these areas (Fig. 9). The more random pattern of surface morphology in E1 relative to E2 is perhaps better illustrated in the Laplacian image than in Fig. 8. The predominately N–S trend of the topography in U1 is also visible in Fig. 9. The large compression ridge at the toe of the landslide complex along the north bank of the Motunau River is also more clearly defined in Fig. 9 than in Fig. 8.

While the Laplacian operator did map many of the interior features of the slide complex correctly, in general it did not differentiate the entire complex from the surrounding terrain as cleanly as did the statistics. There was more confusion with both fine scale topography caused by overland flow and rilling and broad undulations on slopes where the dominant modern surface process appears to be soil creep. Examples of the latter are visible in Fig. 9 in the area west of the landslide.

6. Spectral analysis

Two-dimensional spectral analyses can be used to quantify the scale-dependence of topographic roughness (Turcotte, 1997). To explore the efficacy of this technique, we calculated the power spectra for a 100×100 m patch of topographic data (with a 1 m grid spacing) for three areas that experienced different histories of landsliding. The 1-m grid spacing assured that topographic features with a length scale of a few meters, which are common within the slide, would be

included in the analysis. Test areas of 100×100 m are the minimum size necessary to still include a good sample of these landslide features. We analyzed a patch in the center of unit E2 characterized by active movement that causes relatively regular folding. The second area is in the central portion of E1 where there appears to be less active movement and less pronounced folding. Finally, a patch of smooth, unfailed terrain just northwest of the main Coringa Landslide was analyzed (located at 2512900E, 5798000N in Fig. 6).

In order to distinguish local roughness from broad topographic trends in each of the three areas, we first subtracted a coarsely smoothed version of the topography from the local elevation data, producing a rough surface with mean elevation equal to zero. The initial step in the smoothing procedure was the definition of points at 2-m intervals within the test patches. Then a second order polynomial was fit to all data within 10 m of each point and the elevation values of the points were established locally according to these polynomial fits. Finally these smoothed data were subtracted from the original gridded laser data to produce a residual surface. Such residual surfaces reveal the form of local deformation features or their absence. As a result, the spectral signature that arises from our analysis is purely associated with local surface features and not general topographic trends. We calculated the two-dimensional power spectra for each residual surface using a radial-based coordinate scheme (Turcotte, 1997). Resulting power spectra illustrate how spectral power (which can be thought of as roughness) varies with wavelength such that, for example, several folds with a highly characteristic length scale within a landslide should produce a distinct spectral peak (Fig. 10).

Coarse-scale topographic data have been shown to exhibit scale invariance over many orders of magnitude, so that the power spectra vary with wavelength according to a power-law equation (Turcotte, 1997). In contrast, our analyses of fine resolution data indicate systematic patterns that deviate from power-law behavior (Fig. 10). For the smooth, unfailed area (labeled S), spectral power increases monotonically with wavelength and no dominant length scale is apparent. In contrast, both earthflow areas E1 and E2 exhibit variable spectral peaks for wavelengths between 9 and 20 m. The distinct peak shown for E2
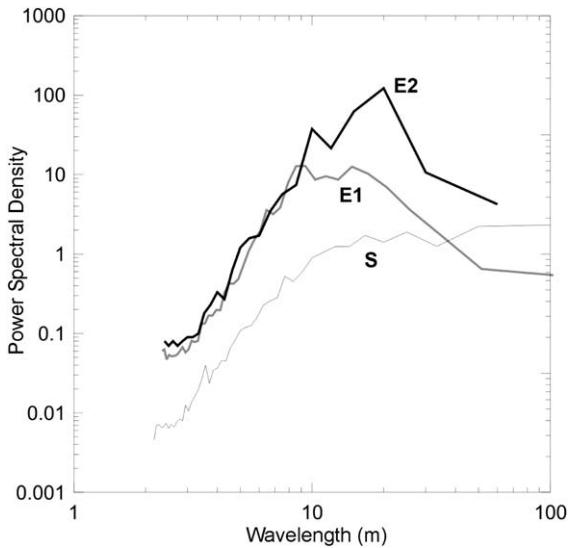
Fig. 10. Power spectra for three 100×100 m sub-areas of the study site (see procedure description in text). Spectral power corresponds to topographic roughness associated with a particular wavelength. No dominant wavelength (or roughness scale) is observed for smooth, unfailed terrain, curve S. The unfailed terrain data are from location 2512900E, 5798000N in Fig. 6. Spectral data from the center of the most active earthflow, curve E2, have a distinct spectral peak with a dominant wavelength of 20 m. The less active and more degraded earthflow, E1, has a broader and lower spectral peak with wavelengths of 9 to 14 m.

suggests the presence of relatively regular spacing of roughness elements, corresponding to the pattern of folding previously discussed. The broader peak associated with E1 indicates a series of similar scale features but without a single characteristic wavelength. One interpretation of Fig. 10 is that the lower and broader peak spectral density in E1 results from smoothing over time of the surface of this less active earthflow. However, we cannot rule out the possibility that the surface of E1 was never as regularly rough as the modern surface of E2.

7. Discussion

7.1. Identifying and mapping the perimeter of bedrock landslides

The results of this pilot study suggest that all of the tested statistics can be used successfully to detect and generally map the area of bedrock landslides and that the exact details of the statistical measure of roughness are less critical. It is more important to have DEMs with appropriate grid resolution to be able to evaluate topographic roughness over a suitable length scale. The Coringa Landslide could not be correctly identified and mapped using a statistical analysis of roughness depicted in a DEM with a standard 25 or 30 m grid resolution.

Having said that, it also obvious that each statistic is sensitive to different topographic roughness elements and thus may work better in some geologic conditions than others. The one-dimensional measure of the local variability of slope gradient fluctuates most along the borders of abrupt topographic change (positions of strong positive or negative slope curvature). It is predicted then that this statistic will be more effective on slides in ''brittle'' materials that deform with sharp edges along shear and tensile failure surfaces. As most shear failure is commonly concentrated on the margins of slides, the one-dimensional statistic will best map the lateral and head scarps of a slide. This metric may be less definitive where mass movement has caused broader gradual changes in topography or roughness has become degraded after movement slowed.

The local changes in topographic aspect mapped by the two-dimensional circular statistics are the same regardless of the degree of change in slope steepness. Therefore, the circular statistics work equally well in very rough to relatively smooth landslides. However, as mentioned, confusion occurs when the terrain contains flat landscape elements that circular statistics interpret as extremely rough. The three-dimensional measures (eigenvalue ratios or three-dimensional resultant) are the best compromise that is sensitive to changes in both slope and aspect. Of these, the eigenvalue ratios may provide more information by indicating whether the local roughness is random, clustered in three-dimensional orientation or girdled (representing some repeating topographic form). More investigation is needed on other slides to determine whether such information is generally useful and what interpretations it supports.

Topographic roughness occurs at all spatial scales, and at any scale, roughness may vary according to the causal geomorphic processes. However, our practical ability to measure roughness in landscapes is limited

to a minimum length scale on the order of meters. A critical and unresolved question is, above this practical minimum limit, what is the appropriate length over which to measure roughness. In this project, the specific issue is the appropriate density of raw LIDAR elevation data necessary to produce DEMs that can be used to detect and map both the perimeter and interior features of bedrock landslides and distinguish the slides from surrounding terrain. In addition, in this study local roughness was often measured in sampling windows, so the evaluated length scale was a function of both grid resolution and window size.

There is little published guidance regarding the best DEM resolution for landslide investigations and we know of none applicable to the style of roughness analysis attempted in this investigation. However, there is a vast literature of studies that document the spacing, scale, and spatial patterns of surface deformations from landslides. From this accumulated knowledge and our own and previous studies of the Coringa Landslide, the original LIDAR data density was chosen to support a DEM with a minimum grid spacing of about 1 m. This limit was set by the desire to detect and map features as small as the compression folds in the interior earthflow E2 and to do so in sampling windows with a minimum width of three pixels. The received data density over much of the landslide complex was slightly poorer than requested. Nevertheless, the data still allowed construction of a DEM with resolution sufficient to detect and map the compression folds (although, using the statistical methods, a grid spacing of 0.5 m was necessary for the best mapping result). By trial-and-error, a variety of grid sizes was produced from the LIDAR data and used with the various roughness measures previously discussed. While this worked in this pilot study, it is clearly not a satisfactory approach for general use over large areas.

In this test area a slightly coarser grid resolution (3 to 4 m) is superior for detecting and mapping the general forms of bedrock landslides using the eigenvalue ratio $\ln(S_1/S_2)$ and the other statistical measures. At this resolution, confusion of the landslides with surrounding unfailed hillslopes appears to be minimized. It is possible to consistently distinguish local topographic roughness caused by mass failures from that due to other processes such as overland flow and surface erosion. For example, a hillslope just

northeast of the northern end of the Evesham Fault is covered with small gullies and rills, producing terrain that appears quite rough in the shaded relief image (Fig. 1). However, the eigenvalue ratio statistic computed over a 9-m length scale has not confused them with the earthflows or even the smaller dip slope landslides along the forested tributaries in the northwestern portion of the study area. The gullies are located at coordinates 2513400E, 5798600N in Fig. 6 and the median eigenvalue ratio in this area of fluvial erosion is 1.97 with a standard deviation of 0.59. Inspection of the pattern of eigenvalue ratio values shows that they are at a minimum of about 1.25 on the tops of interfluves and along channels where there are opposing slopes. The majority of the surface of this area is the smooth hillslopes between drainage divides and channels, and on these slopes the ratio rises quickly to about 2.75. In contrast, the median eigenvalue ratio for the entire Coringa Landslide is 1.13 with a standard deviation of 0.63.

When the grid resolution was dropped to 1 m, confusion increased using the eigenvalue ratio $\ln(S_1/S_2)$ as very local roughness on the scale of 3 m was identified in many areas outside the landslide. Conversely, if the resolution was coarsened to 7 m and the roughness was evaluated in a 21-m-wide sample window, the perimeter of the landslide complex could not be very accurately mapped.

The trial-and-error approach to selection of grid resolution and sampling window size for the statistical and Laplacian analyses is cumbersome and somewhat subjective, although generally successful in this project. The spectral analysis is a more efficient technique that objectively explores length scale dependence and defines any dominant wavelengths of roughness. Work is continuing to explore the application of spectral analyses to landslide detection and mapping.

7.2. Interpreting landslide kinematics and mechanics

Most large bedrock slide complexes, like the Coringa Landslide, are composed of several internal compartments of material that are moving semi-independently of neighboring compartments. Identification and mapping of these kinematic units is often key to understanding the mechanics and behavior of the overall landslide and its likely response to changes in land use or environmental conditions.

At the Coringa slide, the Blocky unit is easily identified and mapped, as noted previously, because of the change in surface roughness caused by the incorporation of a different material, the blocks of Amuri Limestone. Variations in roughness among units U1, E1 and E2, however, appear to be the result of slide mechanics and the degree of recent slide activity within each of these units, as the materials in all three are similar. The boundaries between U1, E1 and E2 are distinct interfaces where levees and small folds have developed. Similar topographic features are common in earthflow landslides but the mechanics of their formation are little studied and poorly understood (e.g. see Fleming and Johnson, 1989; Baum et al., 1993 for discussions of the possible origins of such levees).

The interior of earthflow E2 appears to contain several separate packages or groups of folds that are mapped by both the eigenvalue ratio and Laplacian operator (Figs. 8 and 9). Historical airphotos suggest that these may be time sequential and represent periods when renewed activity in the source area of E2 caused material to surge through the narrow transportation track visible in Fig. 3 and then slow down in the depositional zone in the lower half of E2. As the packages of material accumulated in the gentler depositional zone, they went into compression and began to fold. The oldest of these packages is between coordinates 5797125N and 5797200N (Figs. 8 and 9). This material is distinguished by the orientation of the folds being more variable with several trending W–E as well as NW–SE.

The best-preserved sequence of transverse folds in E2 is the group in the packet of slide debris between 5797200N and 5797300N in E2. In this area, the trend of folding is much more consistently NW–SE. The location of a profile perpendicular to the axes of four folds in this region is shown in Figs. 8 and 9 and the profile is plotted in Fig. 11a and b. These folds are extremely regular with a wavelength of about 11 m and amplitude of about 0.5 m. Fig. 11a also illustrates the performance of the eigenvalue ratio $\ln(S_1/S_2)$. The ratio declines over both fold crests and troughs and rises on the intervening smooth slopes. Thus in Fig. 8, pairs of lines of high roughness correspond to an adjacent fold crest and trough. The performance of the Laplacian operator over the same four folds in area E2 is shown in Fig. 11b. The Laplacian values
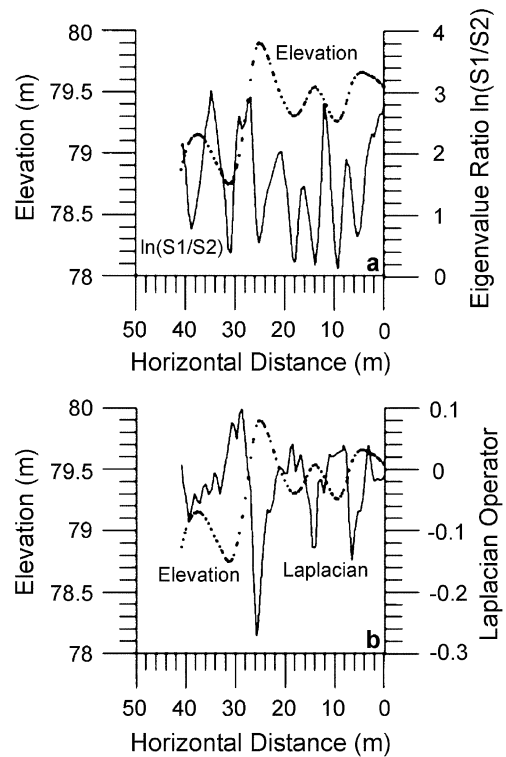

Fig. 11. Details of fold geometry and surface roughness along the profile location shown in Figs. 8 and 9. (a) shows the eigenvalue ratio $\ln(S_1/S_2)$ and (b) the Laplacian operator. The dotted lines indicate the surface topography of four small folds with a wavelength of 10–13 m in the earthflow E2. The eigenvalue ratio declines over the rough topography caused by either fold crests or troughs and increases over the smooth slopes on the sides of the folds. The Laplacian values are low over the convex fold crests.

accurately map and differentiate both the fold crests and troughs.

Fig. 11 also demonstrates the importance of the length scale over which roughness is evaluated. The LIDAR data and detailed ground surveying show that the wavelength of these folds is a nearly constant 11 m. The width (measured horizontally) of the convexity at each crest and the concavity at each trough is about 3.5 to 4 m. The horizontal length of the smooth slopes between fold crests and troughs is typically 2 to 3 m. The statistical measures used in this study must map all three of these topographic components to be able to accurately define the folds. Experimentation revealed that suitable accuracy (evaluated visually) was achieved when the length scale of evaluated roughness was about one-half the horizontal dimen-

sion of these components. Thus, with a minimum sample window size of three cells-by-three cells, the grid spacing had to be 0.5 m. The Laplacian operator maps convexities or concavities and does not need to distinguish the smooth slopes between a fold crest and trough. Therefore, the grid size was successfully increased to 1 m for the Laplacian analysis.

Between 5797300N and 5797400N in E2 (Figs. 8 and 9) is a region with diverse folding orientations. This area has a very distinct southern boundary along a broad compression ridge that trends NW–SE and then turns sharply SW–NE. The region between 5797400N and 5797550N in E2 is a quite complicated zone where material exiting the narrow transportation track makes an abrupt approximately 70° left turn followed by an equally abrupt 60° right turn (see also Fig. 3). This transition occurs over a downslope distance of about 50 m, during which the slope of the moving debris declines from 11% to about 8% as noted previously. Such complex movement produces a wide array of fold trends. Several other lobes of debris that are oriented along the downslope axis of E2 and located on the true right margin of E2 are also particularly prominent. On historical airphotos, these lobes appear to be locked in place and perhaps represent an earlier period when transport was straight from the narrow track into the depositional area without the modern left and right turns.

Mechanistic interpretations of the style and degree of surface roughness of landslides are rare. Work has begun at the Coringa slide to investigate the mechanics of the nearly constant wavelength and amplitude folding visible in earthflow E2, and to a lesser extent E1. A trench was excavated through the four folds along the profile shown in Fig. 11. All of the folds appear to be thrust-propagated structures with multiple generations of thrust faults visible in each fold (Bird, McKean and Pettinga, in preparation). Modelling is underway to explore the relationships between fold geometry, depth to a basal shear surface, and material properties. The goal of the research is to determine if in this case detailed maps of surface topography can be interpreted to approximately predict the material properties, mechanics, and depth of the earthflows in the landslide complex.

It is tempting to predict the future behavior of a slide like Coringa based on the spatial patterns of surface roughness. Indeed, one might argue that all

other things being approximately constant, the most recently active zones within a single slide, or the most recently active slide within a group of slides, will be topographically rougher. In many earth materials, mechanical failure causes deformations with relatively sharp boundaries. When failure ceases or slows, the boundaries of deformation are smoothed over time by a variety of processes. Surface roughness can certainly be quantified using measures like those presented here and thus maps produced of relative activity over some recent past period. However, it is not appropriate to conclude that a smoother compartment within a single slide, or a smoother slide among several failures in similar geologic conditions, is "safer". An estimate of safety is in fact a prediction of future behavior, while surface roughness is a reflection of past activity. Such predictions of behavior should only be based on sound understanding of landslide mechanics. What we propose here is that in some cases, measuring and mapping surface roughness in high resolution DEMs can improve our understanding of landslide mechanics and contribute to better predictions of the likely response of a bedrock landslide to changes in its physical environment.

7.3. Other new technologies

Both airborne SAR imagery and radar interferometry have also shown great potential for landslide studies, particularly for defining zones of deformation within a slide (e.g. Singhroy, 1995; Fruneau et al., 1996; Singhroy et al., 1998; Kimura and Yamaguchi, 2000). Multi-pass radar interferograms can map small time-sequential relative topographic displacements on the order of 1 cm (Fruneau et al., 1996). However, calibration with field-monitored data is normally needed to define absolute movements (Fruneau et al., 1996; Kimura and Yamaguchi, 2000). Interferometry can also be complicated by changes over time in atmospheric water vapor (Kimura and Yamaguchi, 2000) or the vegetation canopy (Fruneau et al., 1996). Loss of radar coherence can also occur if there has been excessive landslide deformation between successive data acquisitions (Carnec et al., 1996). It is unknown how well landslide displacements can be evaluated in multi-temporal DEMs produced from LIDAR data, and such work is planned at the Coringa Landslide test site.

Radar shadowing can be an issue in steep, rugged terrain and the combination of slope aspect and steepness and radar acquisition angle can strongly affect the resolution of radar data (e.g. Carnec et al., 1996). Airborne LIDAR data are gathered over a narrow vertical swath angle (usually less than 20° off nadir) and normally do not suffer from topographic shadowing. LIDAR data are also much easier to process than SAR information and the data can be obtained with a density on the order of 1 m and vertical accuracy on the order of 10 cm. LIDAR derived DEMs can have a grid resolution approaching 1 m and a vertical accuracy of about 20–30 cm depending on the instrumentation, operator skill, and topographic roughness. Singhroy et al. (1988) indicates that typical DEMs produced by single-pass airborne interferometry will have a grid resolution of 5 to 10 m with an accuracy of 1 to 5 m RMS and a height bias of usually less than 10 m.

8. Conclusions

Previous landslide field investigations have typically been either very detailed geotechnical studies of specific sites or more generalized, often subjective, mapping-based evaluations of slides over larger areas. New technologies now allow us to digitally map landforms, including landslides, over large areas with unprecedented resolution and accuracy. We have explored techniques to objectively derive information about the spatial extent, internal kinematics and relative activity of bedrock landslides from high resolution DEMs constructed from LIDAR data.

Our initial results show that local surface roughness can be accurately measured from high resolution DEMs. Contrasts in roughness can be interpreted to identify bedrock landslides, map their spatial extent and patterns of occurrence in a landscape and investigate landslide internal kinematics. Statistics can readily be used to quantify roughness over specified length scales. On the relatively gentle terrain of earthflows, such as those within the Coringa Landslide complex, roughness measured over a few meters is most obviously manifested by a change in aspect and all tested statistics that incorporated measures of aspect performed well. None of the statistical measures, as defined in this project, can differentiate between convex and concave landforms. The spher-

ical statistics could easily be adapted to do so by identifying whether the unit vectors were converging or diverging toward the center of the sampling window to define a concavity or convexity, respectively. Alternatively, the Laplacian operator can be used to map convexities and concavities. Using statistical measures of roughness, the grid spacing of a DEM should be about one-half the minimum surface dimension of a landform to allow detection and mapping of the feature.

There are clearly different scales and degrees of roughness within the Coringa Landslide that reflect changes in material properties, movement mechanics and level of activity. Characteristic patterns of deformation were readily revealed using two-dimensional spectral analyses, which may facilitate investigations linking landslide mechanics and surface morphology. Broad areas of compression contain small surface folds, while a constricted zone of rapid material transport is much smoother. The boundaries between kinematic units are localized sites of intensive differential movement that causes rough topography. Further research is needed to investigate more quantitative interpretations of the causes of roughness patterns. Work is underway to study the mechanics of the extremely regular pattern of folding in unit E2 of the Coringa Landslide. A monitoring system is also in place to investigate the evolution of the folds and the relative and absolute motions of the four kinematic units in the slide complex.

Careful monitoring is normally required to accurately establish the activity of slides. However, this is quite expensive and requires sufficient time for movement rates and patterns to be revealed. The expenditure of such time and resources is only warranted on particular critical slope failures. Traditionally the relative activity of bedrock slides in a landscape is established by subjective observations of the "freshness" of surface features. The simple theory being that when active movement slows, surface processes begin to smooth the sharp edges of the landslide topography. However, the subjective smoothness criteria and their application vary among investigators. The techniques presented here allow an automated, rapid, objective measurement of the roughness of landslide topography. Further research is needed to investigate how direct the link is between recency and amount of movement, which together define the state

of recent activity, and surface roughness in the large variety of bedrock landslides.

References

Aleotti, P., Chowdhury, R., 1999. Landslide hazard assessment: summary review and new perspectives. Bull. Eng. Geol. Environ. 58, 21–44.

Anderson, R.S., 1994. Evolution of the Santa Cruz Mountains, California, through tectonic growth and geomorphic decay. J. Geophys. Res. 99, 20161–20179.

Baltsavias, E., 1999. A comparison between photogrammetry and laser scanning. ISPRS J. Photogramm. Remote Sens. 54, 83–94.

Barrell, D.J., 1989. Geomorphic Evolution and Engineering Geological Studies at Coastal Motunau, North Canterbury. Unpublished MSc Thesis, Department of Geological Sciences, University of Canterbury, Christchurch, New Zealand.

Baum, R.L., Fleming, R.W., 1991. Use of longitudinal strain in identifying driving and resisting elements of landslides. Geol. Soc. Amer. Bull. 103, 1121–1132.

Baum, R.L., Fleming, R.W., Johnson, A.M., 1993. Kinematics of the Aspen Grove Landslide, Ephraim Canyon, central Utah. U.S. Geol. Surv. Bull. 1842-F, F1–F34.

Blaschke, P.M., Trustrum, N.A., Hicks, D.L., 2000. Impacts of mass movement erosion on land productivity: a review. Prog. Phys. Geogr. 24, 21–52.

Burbank, D.W., Leland, J., Fielding, E., Anderson, R.S., Brozovic, N., Reid, M.R., Duncan, C., 1996. Bedrock incision, rock uplift and threshold hillslopes in the northwestern Himalayas. Nature 379, 505–510.

Carnec, C., Massonnet, D., King, C., 1996. Two examples of the use of SAR interferometry on displacement fields of small spatial extent. Geophys. Res. Lett. 23, 3579–3582.

Cendrero, A., Dramis, F., 1996. The contribution of landslides to landscape evolution in Europe. Geomorphology 15, 191–211.

Densmore, A.L., Hovius, N., 2000. Topographic fingerprints of bedrock landslides. Geology 28, 371–374.

Densmore, A.L., Ellis, M.A., Anderson, R.S., 1998. Landsliding and the evolution of normal fault-bounded mountains. J. Geophys. Res. 103, 15203–15220.

Fara, H.D., Scheiddegger, A.E., 1963. An eigenvalue method for the statistical evaluation of fault plane solutions of earthquakes. Seismol. Soc. Am., Bull. 53, 811–816.

Fisher, N.I., 1993. Statistical Analysis of Circular Data. Cambridge Univ. Press, Cambridge. 277 pp.

Fisher, N.I., Lewis, T., Embleton, B.J.J., 1987. Statistical Analysis of Spherical Data. Cambridge Univ. Press, Cambridge. 329 pp.

Fleming, R.W., Johnson, A.M., 1989. Structures associated with strike–slip faults that bound landslide elements. Eng. Geol. 27, 39–114.

Fruneau, B., Achache, J., Delacourt, C., 1996. Observation and modelling of the Saint-Étienne-de-Tinée landslide using SAR interferometry. Tectonophysics 265, 181–190.

Gonzalez-Diez, A., Remondo, J., Diaz de Teran, J., Cendrero, A., 1999. A methodological approach for the analysis of the temporal occurrence and triggering factors of landslides. Geomorphology 30, 95–113.

Hobson, R.D., 1972. Surface roughness in topography: a quantitative approach. In: Chorley, R.J. (Ed.), Spatial Analysis in Geomorphology. Methuen & Co., London, pp. 221–245.

Hovius, N., Stark, C.P., Allen, P.A., 1997. Sediment flux from a mountain belt derived by landslide mapping. Geology 25, 231–234.

Hutchinson, J.N., 1995. Landslide hazard assessment. In: Bell, D.H. (Ed.), Proceedings of the VI International Symposium on Landslides, Christchurch, New Zealand, pp. 1805–1841.

Justice, T.R., 1994. Engineering Geologic Investigations of Two North Canterbury Landslide Complexes. Unpublished MSc Thesis, Department of Geological Sciences, University of Canterbury, Christchurch, New Zealand.

Kelsey, H.M., 1980. A sediment budget and an analysis of geomorphic processes in the Van Duzen River basin, north coastal California, 1941–1975. Geol. Soc. Amer. Bull. 91, 1119–1216.

Kimura, H., Yamaguchi, Y., 2000. Detection of landslide areas using satellite radar interferometry. Photogr. Eng. Remote Sens. 66, 337–344.

Kraus, K., Pfeifer, N., 1998. Determination of terrain models in wooded areas with airborne laser scanner data. ISPRS J. Photogramm. Remote Sens. 53, 193–203.

Lang, A., Moya, J., Corominas, J., Schrott, L., Dikau, R., 1999. Classic and new dating methods for assessing the temporal occurrence of mass movements. Geomorphology 30, 33–52.

Latypov, D., 2002. Estimating relative LIDAR accuracy information from overlapping flight lines. ISPRS J. Photogramm. Remote Sens. 56, 236–245.

Moar, N.T., 1971. Contributions to the Quaternary history of the New Zealand flora: Aranuian pollen diagrams from Canterbury, Nelson, and North Westland, South Island. N.Z. J. Bot. 9, 80–145.

Molloy, B., Burrows, C., Cox, J., Johnston, J., Wardle, P., 1963. Distribution of subfossil forest remains, eastern South Island, New Zealand. N.Z. J. Bot. 1, 68–77.

Palmquist, R.C., Bible, G., 1980. Conceptual modelling of landslide distribution in time and space. Bull. Int. Assoc. Eng. Geol. 21, 178–186.

Scheidegger, A.E., 1965. On the statistics of the orientation of bedding planes, grain axes, and similar sedimentological data. U. S. Geol. Surv. Prof. Pap. 525-C, 164–167.

Schmidt, K.M., Montgomery, D.R., 1995. Limits to relief. Science 270, 617–620.

Schuster, R.L., 1996. Socioeconomic significance of landslides. In: Turner, A.K., Schuster, R.L. (Eds.), Landslides: Investigation and Mitigation. Trans. Res. Board, Spec. Rep., vol. 247. National Academy Press, Washington, DC, pp. 12–35.

Selby, M.J., 1993. Hillslope Materials and Processes. Oxford Univ. Press, New York.

Singhroy, V., 1995. SAR integrated techniques for geohazard assessment. Adv. Space Res. 15, 67–78.

Singhroy, V., Mattar, K., Gray, A., 1998. Landslide characterisation in Canada using interferometric SAR and combined SAR and TM images. Adv. Space Res. 21, 465–476.

Turcotte, D.L., 1997. Fractals and Chaos in Geology and Geophysics. Cambridge Univ. Press, Cambridge. 398 pp.

Varnes, D.J., IAEG Commission on Landslides, 1984. Landslide hazard zonation—a review of principles and practice UNESCO, Paris. 64 pp.

Watson, G.S., 1966. The statistics of orientation data. J. Geol. 74, 786–797.

Wills, C.J., McCrink, T.P., 2002. Comparing landslide inventories: the map depends on the method. Environ. Eng. Geosci. VIII (4), 279–293.

Wieczorek, G., 1984. Preparing a detailed landslide-inventory map for hazard evaluation and reduction. Bull. Assoc. Eng. Geol. 21 (3), 337–342.

Woodcock, N.H., 1977. Specification of fabric shapes using an eigenvalue method. Geol. Soc. Amer. Bull. 88, 1231–1236.

Woodcock, N.H., Naylor, M.A., 1983. Randomness testing in three-dimensional orientation data. J. Struct. Geol. 5, 539–548.

Zevenbergen, L.W., Thorne, C.R., 1987. Quantitative analysis of land surface topography. Earth Surf. Processes Landf. 12, 47–56.